

Increase in Precipitation Efficiency with Surface Warming in Radiative-Convective Equilibrium

Nicholas J. Lutsko¹, Timothy W. Cronin¹

¹Department of Earth, Atmospheric, and Planetary Sciences, Massachusetts Institute of Technology,
Cambridge, Massachusetts

Key Points:

- The precipitation efficiency is investigated in RCE simulations with a CRM forced by a wide range of SSTs.
- Precipitation efficiency generally increases with warming because of increased cloud density.
- Changes in the large-scale circulation can cause precipitation efficiency to decrease.

12 **Abstract**

The precipitation efficiency of convection (ϵ) plays an important role in simple models of the tropical atmosphere as well as in global climate models' projections of future climate changes, but remains poorly understood and poorly constrained. A particularly urgent question is how ϵ will change in warmer climates. To address these issues, this study investigates the precipitation efficiency in simulations of radiative-convective equilibrium with a cloud-resolving model forced by a wide range of sea-surface temperatures (SSTs). Two different domains are considered: a small, doubly-periodic domain and a 2D (x - z) "mock-Walker" domain with a sinusoidal SST profile that resembles the equatorial Pacific, and the sensitivities of the results to the microphysical scheme and to the horizontal resolution are also explored. It is found that ϵ generally increases with warming in the small-domain simulations because of increases in the efficiency with which cloud condensate is converted into precipitation, with changes in the re-evaporation of falling precipitation playing a secondary role. This picture is complicated in the 2D simulations by substantial changes in the degree of convective organization as the underlying SSTs are varied, which impact the relative fractions of low clouds, which have small (≤ 0.1) precipitation efficiencies, and of high clouds, which have larger (~ 0.4) precipitation efficiencies.

30 **1 Introduction**

The precipitation efficiency of convection is a measure of how much of the water that condenses in a rising column of air reaches the surface as precipitation, and can be defined as $\epsilon = P/C$, where P is the surface precipitation rate (with units $\text{kg m}^{-2}\text{s}^{-1}$) and C is the column-integrated condensation rate (also $\text{kg m}^{-2}\text{s}^{-1}$). ϵ can be defined at various temporal and spatial scales (see *Sui et al. [2007]*), and in what follows we primarily focus on the tropical-mean, or bulk, precipitation efficiency. Many factors contribute to the precipitation efficiency, particularly the various microphysical processes responsible for the formation and re-evaporation of precipitation, as well as cloud-scale dynamics such as entrainment rates, and we do not currently have a good understanding of what sets ϵ , nor of how its value will change in future climates.

Despite this uncertainty, precipitation efficiency can be tuned quite precisely in some global climate models (GCMs, *Zhao [2014]*), and several recent studies have found a strong

relationship between climate sensitivity and the response of ϵ to warming (*Mauritsen et al.* [2012]; *Zhao* [2014]; *Tomassini et al.* [2015]; *Zhao et al.* [2016]). This correlation is thought to come from the effect of ϵ on clouds, as models in which the precipitation efficiency decreases in warmer conditions are able to maintain greater amounts of cloud cover and thus have a more negative cloud feedback (*Zhao* [2014]; *Sherwood et al.* [2014]). *Zhao et al.* [2016] were able to make a single model's cloud radiative effect (CRE) span the CMIP5 intermodel range in CRE by altering the scheme by which cloud condensate is removed as precipitation, with no discernible impact on the quality of the GCM's representation of the present-day climatology. In addition to this relationship with climate sensitivity, ϵ is also an important factor in models' projections of future changes in the hydrologic cycle, and influences the rate at which aerosols are removed from the atmosphere [*Bailey et al.*, 2015].

From a more theoretical point of view, precipitation efficiency is often a key parameter in simple models of the dynamics of the tropical atmosphere. In idealized models of the tropical atmosphere the updraft mass fraction, M_u , is often related to the downdraft mass fraction, M_d , by (*Emanuel* [1987]; *Yano and Emanuel* [1991])

$$M_d = -(1 - \epsilon)M_u, \quad (1)$$

which linearly interpolates between the two limits of downdrafts cancelling the mass transported by updrafts, resulting in the net convective mass flux being zero ($\epsilon = 0$ and so $M_d = -M_u$), and of there being no downdrafts in convecting regions ($\epsilon = 1$ and so $M_d = 0$). Using this relationship, it has been shown that high values of ϵ promote radiative-convective instability [*Emanuel et al.*, 2014]¹, and that the gross moist stability, or proportionality between column moisture convergence and column energy divergence, depends strongly on the precipitation efficiency [*Raymond et al.*, 2009]. ϵ also influences how effectively the heat transported upwards by moist convection is converted to mechanical energy dissipation by winds. If ϵ is very small, this conversion can approach the limit of a perfect heat engine (*Emanuel and Bister* [1996]; *Rennó and Ingersoll* [1996]), whereas for more realistic precipitation efficiencies moist convection also works to de-

¹ A caveat is that this study ignored variations in relative humidity; high precipitation efficiency is associated with drier atmospheres which are less susceptible to radiative-convective instability, so the actual dependence of instability on ϵ is complex.

70 humidify the atmosphere, so the conversion of heat transport to wind energy dissipation
 71 is reduced [Pauluis and Held, 2002a].

72 Given the impact of precipitation efficiency on future climate projections, the fact
 73 that it can be prescribed in GCMs and its importance for our conceptual understand-
 74 ing of the tropical atmosphere, better constraints are needed on its value and on how this
 75 value might change in a warmer world. These constraints must be obtained from a com-
 76 bination of focused modelling studies and observations, and would directly inform de-
 77 velopment of the convective parameterizations used in GCMs. As a first step towards
 78 this goal, in this study we have investigated how the precipitation efficiency varies in sim-
 79 ulations of radiative-convective equilibrium (RCE) with a cloud-resolving model (CRM)
 80 as the underlying sea-surface temperature (SST) is varied. We consider both doubly-periodic,
 81 small domain simulations and 2D “mock-Walker Cell” simulations, which include hor-
 82 izontal SST gradients and so allow us to investigate how ϵ is affected by the presence of
 83 a large-scale circulation.

84 To our knowledge, the only theoretical constraint on ϵ comes from Romps [2014],
 85 who showed that in the entraining plume model with condensation

$$\epsilon(z) \geq 1 - RH(z), \quad (2)$$

86 where z is height and RH is the relative humidity. This is not a very stringent constraint
 87 however, and applies only when convection behaves as a single entraining plume. In sim-
 88 ulations Romps found that ϵ was sometimes twice as large as the $1 - RH$ lower bound.
 89 More speculatively, it has been suggested that an increase in convective aggregation with
 90 warming could increase precipitation efficiency [Mauritsen and Stevens, 2015], but sim-
 91 ulations of convective aggregation show inconsistent tendencies with surface warming (Wing
 92 and Emanuel [2014]; Coppin and Bony [2015]; Cronin and Wing [2017]), and the changes
 93 in bulk precipitation efficiency in models resulting from convective aggregation have not
 94 been carefully examined.

95 In large-eddy simulations (LES) of individual cumulus congestus clouds, Langhans
 96 et al. [2015] found precipitation efficiencies between 0.3 and 0.4, and demonstrated that
 97 the “sedimentation efficiency” (the probability of a falling hydrometeor reaching the sur-
 98 face) is the dominant control on precipitation efficiency in their model. In coarser-resolution
 99 simulations of RCE with CRMs, ϵ is typically found to be between about 0.2 and 0.5 (e.g.,
 100 Pauluis and Held [2002b]; Tao et al. [2004]; Romps [2011]), but no systematic investi-

101 gation of what sets the value of ϵ nor of how ϵ varies with warming has been carried out
 102 in models of this type.

103 Precipitation efficiency is difficult to measure observationally. *Lau and Wu* [2003]
 104 used satellite retrievals of rainfall and cloud liquid water to demonstrate that the pre-
 105 cipitation efficiency of warm rain increases as the underlying SST increases, but this re-
 106 sult required the use of a microphysical parameterization to convert the satellite data
 107 into precipitation efficiencies. Recently, *Bailey et al.* [2015] used water vapor isotope ra-
 108 tios to measure ϵ near Hawaii's Big Island and found that synoptic weather plays an im-
 109 portant role in setting the precipitation efficiency, with different types of weather sys-
 110 tems having very different efficiencies.

111 None of these studies have provided the parameter-dependence of ϵ needed by GCMs,
 112 however, and characterizing the precipitation efficiencies in our CRM simulations is an
 113 important intermediate step towards obtaining this goal. With the CRM, we are able
 114 to perform a large number of simulations to investigate the sensitivity of ϵ in our model
 115 to the underlying SST, the microphysical scheme, the horizontal grid resolution and the
 116 presence of a large-scale circulation. We have also used a similar framework to *Langhans*
 117 *et al.* [2015] to diagnose the factors which determine ϵ , providing a physical explanation
 118 for why ϵ varies as it does.

119 The model, experiments and diagnostic framework are presented in the next sec-
 120 tion. The results of the small domain experiments are presented in section 3 and the 2D
 121 mock-Walker simulations are discussed in section 4. We end with a summary and con-
 122 clusion in section 5.

123 2 Methods

124 2.1 Model and Experiments

125 The cloud-resolving model is version 6.10.8 of the System for Atmospheric Mod-
 126 eling (SAM, *Khairoutdinov and Randall* [2003]). This model solves the anelastic conti-
 127 nuity, momentum, and tracer conservation equations, and its prognostic thermodynamic
 128 variables are liquid/ice water static energy, total nonprecipitating water (vapor, cloud
 129 water and cloud ice), and total precipitating water (rain, snow and graupel).

130 All simulations were conducted without rotation and with fixed SSTs. The small
 131 domain simulations were performed on a square, doubly periodic domain, with width 96km.
 132 The mock-Walker simulations were performed on a 2D ($x - z$) domain, periodic in x
 133 and with length 24576km. In both set-ups the vertical grid has 64 levels, starting at 25m
 134 and extending up to 27km, and the vertical grid spacing increases from 50m at the low-
 135 est levels to roughly 1km at the top of the domain. Gravity waves are damped at the
 136 top of the domain and subgrid-scale fluxes are parameterized using Smagorinsky's eddy
 137 diffusivity model. We will focus on results from simulations which used a grid size of 1km
 138 for the small square domain and 3km for the 2D Walker domain, but have also explored
 139 the sensitivity of our results to the horizontal resolution (section 3.4).

140 A variable time-step is used, with maximum interval 10s, and radiative fluxes are
 141 calculated every 40 time-steps using the CAM radiation scheme. The incoming solar ra-
 142 diation is fixed at 650.83 W m^{-2} with a zenith angle of 50.5° , and the simulations were
 143 initialized with a small amount of white noise added to the temperature field near the
 144 surface to initiate convection.

145 Greenhouse gases are fixed at present day levels and the mean SST is varied in in-
 146 crements of 2.5K from 290K to 310K in both set-ups. Simulations with SSTs less than
 147 300K were run for 150 days, with averages taken over the last 50 days. The simulations
 148 with higher SSTs equilibrated more quickly and so these were run for 100 days and av-
 149 erages were again taken over the last 50 days. The SSTs in the mock-Walker simulations
 150 have a sinusoidal profile, with the difference between the warmest SSTs (plotted in the
 151 center of the domain) and the coldest SSTs kept fixed at 5K, which creates a compara-
 152 ble SST gradient to the equatorial Pacific.

153 Three sets of simulations were performed with each set-up in order to test the sen-
 154 sitivity of ϵ to the microphysical scheme. Two sets of simulations used the single-moment
 155 microphysics scheme implemented in SAM by *Khairoutdinov and Randall* [2003]; one with
 156 the original parameter settings described by *Khairoutdinov and Randall* [2003] and one
 157 with the "NOSEDAALIQ5" set-up of *Lopez et al.* [2009]. In this configuration there is
 158 no ice sedimentation, the ice autoconversion threshold is lowered by a factor of 100, and
 159 the autoconversion and accretion rates for liquid water are increased by a factor of five.
 160 *Harrop and Hartmann* [2016] showed that this configuration produces more realistic at-
 161 mospheric cloud radiative heating profiles than the original configuration of *Khairout-*

¹⁶² *dinov and Randall* [2003]. We will refer to the two sets of single-moment simulations as
¹⁶³ the “K03” and “NA5” simulations, respectively. The third set of simulations used the
¹⁶⁴ double-moment scheme of *Morrison et al.* [2005], and will be referred to as the “M05”
¹⁶⁵ simulations.

¹⁶⁶ The original formulation of the double-moment scheme includes prognostic param-
¹⁶⁷ eterizations for supersaturation and droplet activation, however the scheme has been mod-
¹⁶⁸ ified to fit SAM by instead partitioning water between the vapor phase and the condensed
¹⁶⁹ phases via a saturation adjustment (i.e., no supersaturation is allowed). This ensures that
¹⁷⁰ temperature, water vapor and cloud liquid water values are consistent throughout SAM’s
¹⁷¹ calculations. The single-moment scheme uses the same saturation adjustment. Follow-
¹⁷² ing saturation adjustment, the condensed water is partitioned between cloud ice, cloud
¹⁷³ liquid water, rain, snow and graupel, and fluxes for each of these are calculated. The con-
¹⁷⁴ densation rate is calculated by subtracting the total condensed water before the satu-
¹⁷⁵ ration adjustment from the condensed water after the saturation adjustment.

¹⁷⁶ In terms of factors that might influence precipitation efficiency, the main differences
¹⁷⁷ between the two schemes are:

- ¹⁷⁸ • In the single-moment scheme the autoconversion of cloud condensate is param-
¹⁷⁹ eterized using the Kessler formulation, which is a fractional removal scheme, and
¹⁸⁰ droplet collection is assumed to follow the continuous growth equations. In the
¹⁸¹ Morrison scheme the autoconversion of cloud droplets to rain is parameterized based
¹⁸² on the numerical simulations of droplet growth by stochastic collection of *Beheng*
¹⁸³ [1994] and the autoconversion of cloud ice to snow is modelled using a vapor dif-
¹⁸⁴ fusion growth rate. The collection of droplets by falling hydrometeors is calculated
¹⁸⁵ using a gravitational collection kernel.
- ¹⁸⁶ • In the single-moment scheme the phase of nonprecipitating and precipitating con-
¹⁸⁷ densates is diagnosed from the temperature; for example, a cloud at 263.15 K is
¹⁸⁸ assumed to be half liquid and half ice. In the Morrison scheme cloud ice is assumed
¹⁸⁹ to melt instantaneously at temperatures above 273.15K and homogeneous freez-
¹⁹⁰ ing of cloud liquid water and rain occurs instantaneously for temperatures below
¹⁹¹ 233.15K, but the phase of condensates between these temperatures is simulated
¹⁹² prognostically by the model.

- In the single-moment scheme the size distributions of precipitating hydrometeors are given by the *Marshall and Palmer* [1948] distributions, while in the Morrison scheme they follow gamma distributions.
- The two schemes have slightly different formulations of the terminal fall velocities of both rain and snow, as well as of the sedimentation rate of cloud ice.
- In both schemes the evaporation of rain and the sublimation of snow are modelled by vapor diffusion, but the formulations are different.

The parameterizations implemented in the Morrison scheme are generally more accurate than those in the K03 scheme, in terms of matching experiments and high resolution numerical simulations (e.g., *Beheng* [1994]), though the improvements are subtle and the increased complexity of the Morrison scheme makes it harder to interpret the relationship between the cloud microphysics and changes in precipitation efficiency.

2.2 Diagnostic Framework

We have used a similar framework to *Langhans et al.* [2015] to diagnose the causes of changes in precipitation efficiency. This consists of decomposing the process of cloud condensate reaching the surface as precipitation into two steps. First, a fraction α of the cloud condensate is converted into precipitation, while $(1 - \alpha)$ stays suspended in the column and either forms a cloud or else is detrained from the convecting region and evaporates. This is the conversion step and we will refer to α as the conversion efficiency. In the second step the precipitation falls to the surface, during which some fraction β is re-evaporated and so we will refer to $1 - \beta$ as the sedimentation efficiency (see the Introduction). The total precipitation reaching the surface is then

$$P = \alpha C(1 - \beta). \quad (3)$$

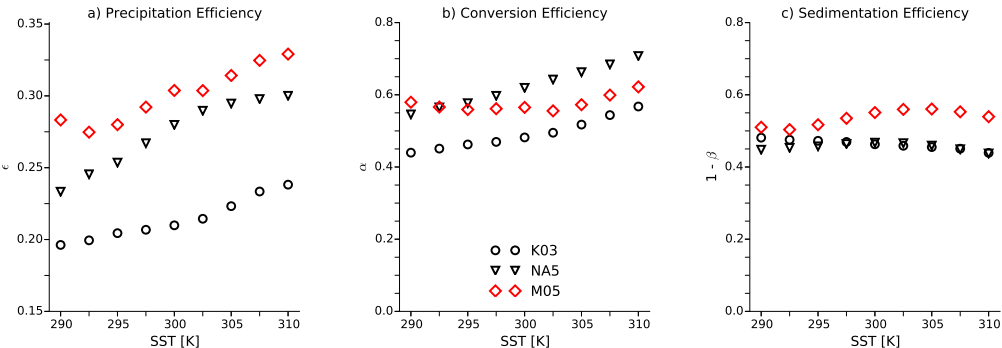
Note that $\beta = E/\alpha C$, where E is the column-integrated sink of precipitation due to evaporation (units $\text{kg m}^{-2}\text{s}^{-1}$). The precipitation efficiency ϵ is

$$\epsilon = \alpha(1 - \beta), \quad (4)$$

and so changes in ϵ can be interpreted by investigating changes in α and β . In general we estimate α and β using domain-averaged values of P , C and E , however we have also calculated “local” values for the mock-Walker simulations (see section 4).

220 **3 Small Domain Simulations**

221 **3.1 Variation of ϵ with SST**



222 **Figure 1.** a) The precipitation efficiency ϵ as a function of SST for the three sets of small
 223 domain simulations. Black circles show results with the single-moment microphysics scheme and
 224 the K03 parameter settings; black triangles show results with the NA5 parameter settings; and
 225 red diamonds show results with the M05 scheme. b) The conversion efficiency α as a function of
 226 SST for the same simulations. c) The sedimentation efficiency $1 - \beta$ as a function of SST for the
 227 same simulations.

228 The precipitation efficiency ϵ is plotted as a function of SST for the three sets of
 229 small domain simulations in Figure 1a. ϵ varies between 0.2 and 0.25 in the K03 sim-
 230 ulations (black circles); between 0.23 and 0.29 in the NA5 simulations (black triangles);
 231 and between 0.27 and 0.33 in the M05 simulations (red diamonds). These values are typ-
 232 ical of small domain RCE simulations (e.g., *Pauluis and Held* [2002b]; *Tao et al.* [2004];
 233 *Romps* [2011]). The precipitation efficiency increases monotonically as the SST is increased
 234 in each set of simulations, with the fractional increase typically around $1\text{-}3\%K^{-1}$, except
 235 that the precipitation efficiency decreases with the M05 scheme when going from 290K
 236 to 292.5K.

237 In both sets of simulations with the single-moment scheme the conversion efficiency
 238 α increases monotonically with SST (Figure 1b), going from 0.45 to 0.58 in the K03 sim-
 239 ulations and from 0.55 to 0.72 in the NA5 simulations. The sedimentation efficiency $1 -$
 240 β decreases slightly in the K03 simulations, from 0.47 to 0.44 (Figure 1c), while it first
 241 increases with warming and then decreases with warming in the NA5 simulations, though
 242 these changes are small. So the increasing precipitation efficiency in these simulations

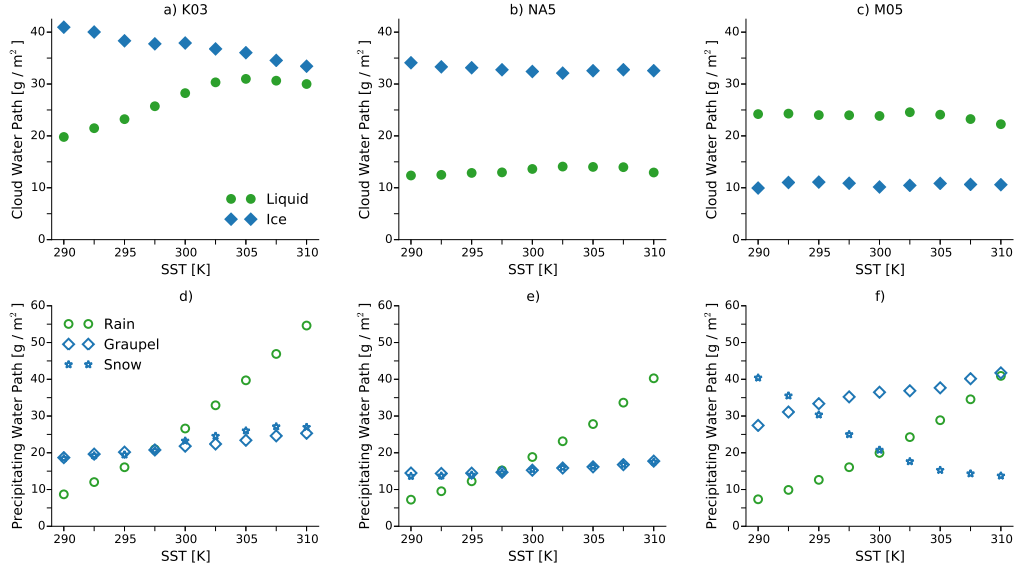
243 is due to the increasing conversion efficiency, which wins out over the small changes in
 244 the sedimentation efficiency.

245 The M05 simulations are more complicated. The conversion efficiency α decreases
 246 for SSTs between 290K and 295K, is stable between 295K and 302.5K, and then increases
 247 again for the warmest SSTs. The sedimentation efficiency $1-\beta$ increases between 292.5K
 248 and 302.5K from about 0.5 to 0.55 and then decreases slightly. Hence the precipitation
 249 efficiency increases between 292.5K and 302.5K because less of the falling precipitation
 250 re-evaporates, countering the reduced conversion efficiency, while for warmer SSTs the
 251 re-evaporation is relatively constant and so the increasing conversion efficiency causes
 252 the precipitation efficiency to increase. The reduction in ϵ between 290K and 292.5K is
 253 due to a reduction in the conversion efficiency, as the re-evaporation is roughly the same
 254 in these two simulations.

255 Comparing the three sets of simulations, the conversion efficiency is smallest in the
 256 K03 simulations and largest in the NA5 simulations, except for the two coldest simula-
 257 tions in which α is larger in the M05 simulations. The sedimentation efficiency is always
 258 larger in the M05 simulations than in the single-moment simulations, and the K03 and
 259 NA5 simulations have similar values of β . So the precipitation efficiency is largest in the
 260 M05 simulations because the smallest fraction of falling precipitation is re-evaporated,
 261 and the precipitation efficiency is lowest in the K03 simulations because cloud conden-
 262 sate is converted into precipitation less efficiently than in the NA5 simulations.

263 3.2 Changes in conversion efficiency

272 To understand the changes in α , we begin by describing the abundances of the dif-
 273 ferent condensed water phases in the small domain simulations. The top panels of Fig-
 274 ure 2 show the liquid and ice cloud water paths for these simulations, and the precip-
 275 itating water paths are shown in the bottom panels. In the single-moment simulations
 276 this suggests that the increases in α at warmer SSTs are primarily caused by increases
 277 in the efficiency with which cloud liquid water is converted into rain, as the mass of rain
 278 increases by a factor of more than five from the coldest to the warmest simulation with
 279 both parameter settings (Figure 2d and e). In the K03 simulations the mass of cloud liq-
 280 uid water only increases by about 50%, while it is relatively constant in the NA5 sim-
 281 ulations (Figure 2a and b). In the K03 simulations the mass of cloud ice decreases by



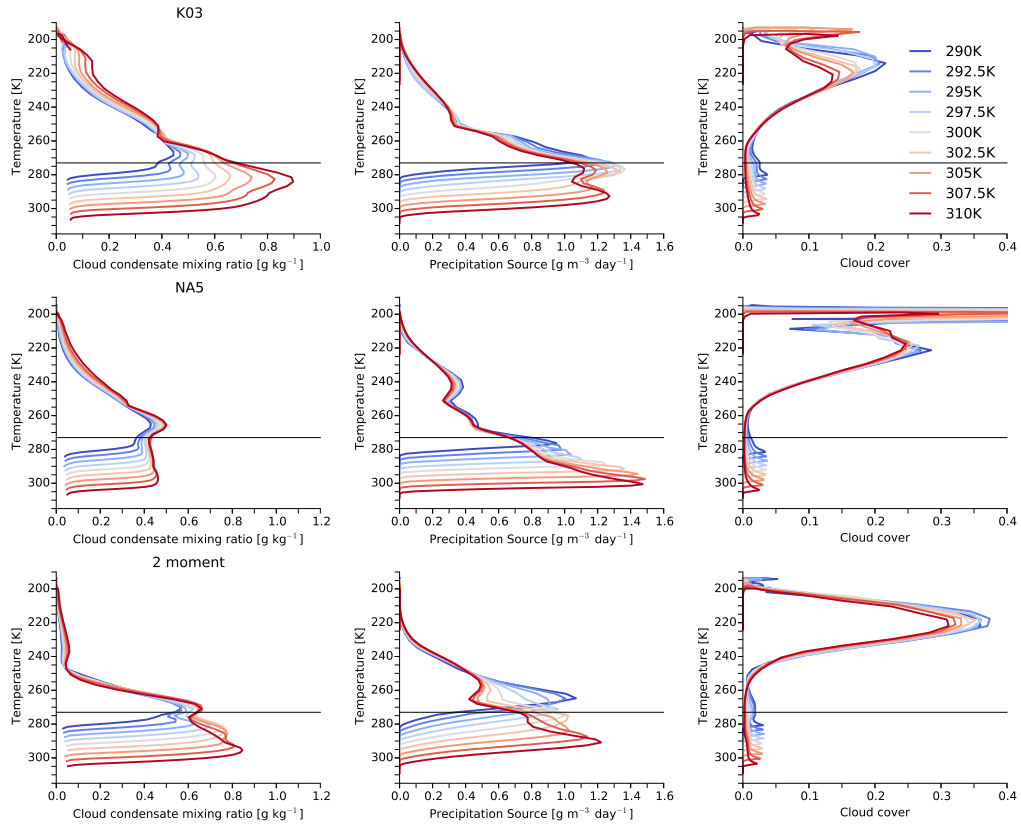
264 **Figure 2.** a) Liquid cloud water path (green circles) and ice cloud water path (blue dia-
 265 phonds) as a function of SST for the small domain simulations with the single-moment scheme
 266 and the K03 parameter settings. b) Same for the simulations with the NA5 parameter settings.
 267 c) Same for the simulations with the M05 scheme. d) Rain path (open green circles), graupel
 268 path (open blue diamonds) and snow path (open blue asterisks) as a function of SST for the
 269 small domain simulations with the single-moment scheme and the K03 parameter settings. e)
 270 Same for the simulations with the NA5 parameter settings. f) Same for the simulations with the
 271 M05 scheme.

282 about 20% over the course of the simulations, but otherwise changes in the masses of the
 283 frozen phases are small.

284 In the single-moment microphysics autoconversion is carried out by a fractional re-
 285 moval scheme, which takes the form

$$\frac{\partial q_p}{\partial t} = \max(0, \eta[q_c - q_{c,0}]), \quad (5)$$

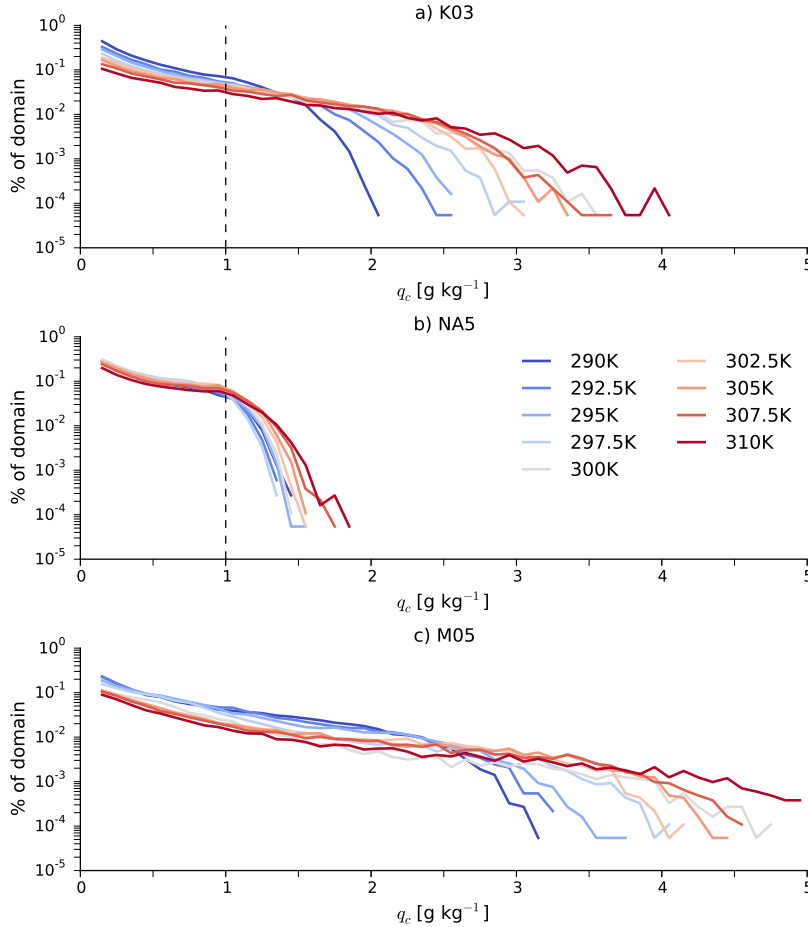
286 where q_p is the mixing ratio of a precipitating species, η is an autoconversion rate co-
 287 efficient, q_c is the mixing ratio of a cloud condensate and $q_{c,0}$ is a threshold condensate
 288 mixing ratio. This equation applies to both liquid and solid phases, though η has a fixed
 289 value for rain and a weak temperature dependence for snow. As a reminder, the value
 290 of η for liquid water is five times larger and the threshold for ice is 100 times smaller in
 291 the NA5 configuration than in the K03 configuration.



292 **Figure 3.** a) Vertical profiles of cloud condensate mixing ratio as a function of temperature
 293 for the small domain simulations with the single-moment scheme and the K03 parameter settings.
 294 The horizontal black line shows the freezing level. b) Profiles of the precipitation source as a
 295 function of temperature for the K03 simulations. c) Profiles of cloud fraction as a function of
 296 temperature for the K03 simulations. d), e) and f) Same for the small domain simulations with
 297 the NA5 parameter settings. g), h) and i) Same for the small domain simulations with the M05
 298 scheme.

299 Denser clouds convert condensation into precipitation more efficiently in this scheme,
 300 and Figure 3a shows that the cloud condensate density increases at almost all heights
 301 as the SST is increased in the K03 simulations. As another way of showing this, prob-
 302 ability density functions (PDFs) of q_c at the altitudes of maximum time-mean conden-
 303 sation are plotted for these simulations in Figure 4a. The PDFs have a consistent struc-
 304 ture across the simulations, decaying exponentially with q_c , before reaching a cut-off value
 305 after which the probability density decays more rapidly. The slopes of the PDFs weaken
 306 and the cut-off values increase as the underlying SST is increased, and both of these changes

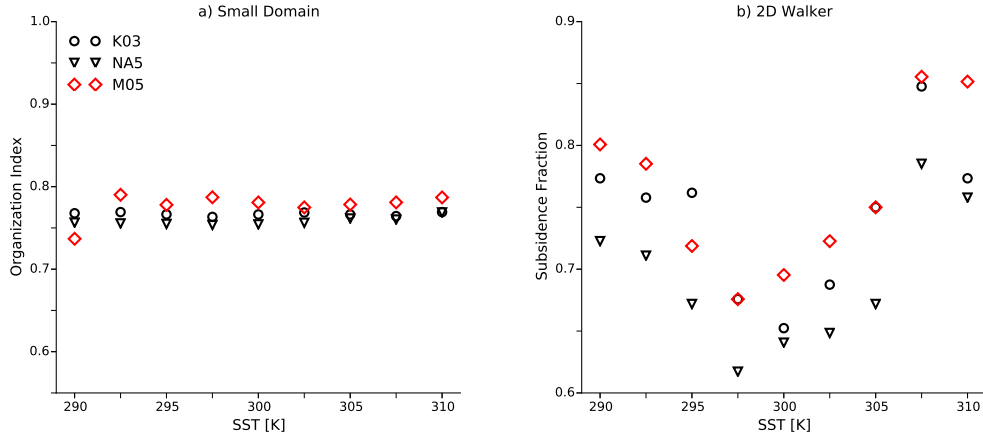
result in a rapid increase in the fraction of the domain that is above the $q_{c,0}$ value for rain (1gkg^{-1}) with surface warming. The fraction of the domain covered by low density ($q_c < q_{c,0}$) clouds decreases as the SST is increased.



310 **Figure 4.** Probability density functions of q_c for the small domain K03 simulations (a), the
311 small domain NA5 simulations (b) and the small domain M05 simulations (c), calculated for the
312 heights at which the maximum time-mean condensation occurs and using 3D files output every
313 hour of the simulations. Note the logarithmic scales for the y-axes. The dashed black lines in the
314 upper two panels show the value of $q_{c,0}$ for liquid rain in the single-moment scheme.

315 Since both the slope and the cut-off change, it is difficult to say what causes the
316 cloud density to increase. One possibility is that the densities increase because the con-
317 viction becomes more organized, with fewer scattered, thin clouds and more deep con-
318 vective towers; however measures of convective organization, such as the subsidence frac-
319 tion (the fraction of the domain with $\omega_{500} > 0$; *Coppin and Bony* [2015]) and the in-

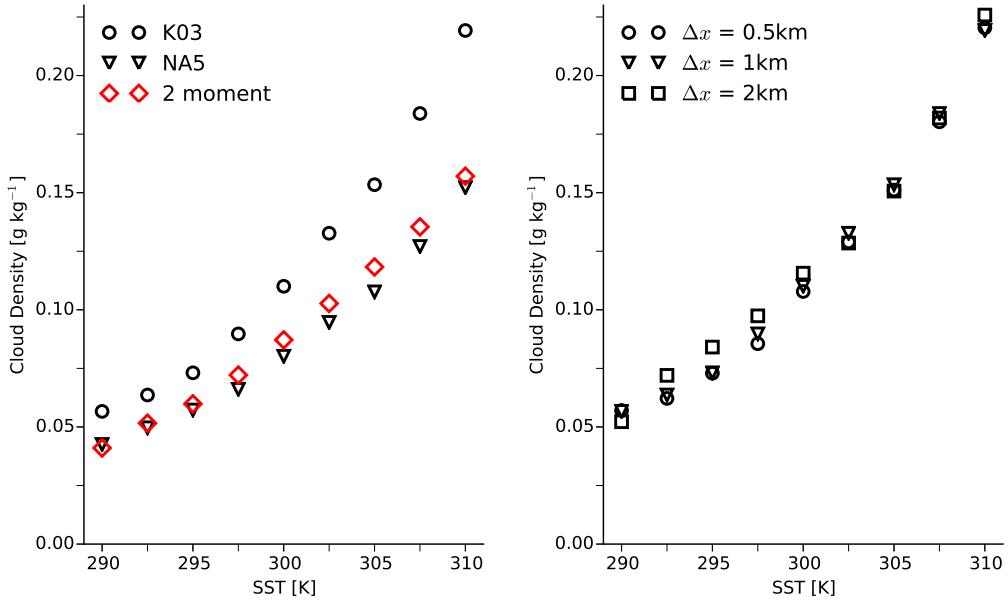
320 dex of convective organization [Tompkins and Semie, 2017], have little variation across
 321 the simulations (Figure 5a).



322 **Figure 5.** a) Index of convective organization averaged over the last 25 days of the small
 323 domain simulations. Black circles show the K03 simulations, black triangles show the NA5 simu-
 324 lations and red diamonds show the simulations with the M05 scheme. b) Subsidence fraction in
 325 the 2D Walker simulations.

326 As an alternative explanation, we note that the mean cloud density increases by
 327 between 2 and 6%K⁻¹ in the K03 simulations (circles in Figure 6a), which is in the range
 328 of values that would be expected for clouds formed by undilute ascent along a moist adi-
 329 abat [Betts and Harshvardhan, 1987]. Although the clouds here are unlikely to be formed
 330 by undilute ascent, the increased availability of water for warmer SSTs probably does
 331 contribute to the increasing cloud density, and in the appendix we provide an argument
 332 for why the density of clouds formed by partially entraining plumes will also increase with
 333 warming, though at a slower rate than clouds formed by undilute plumes.

339 The cloud condensate mixing ratios are smaller in the NA5 simulations (Figure 3d)
 340 and have a different vertical profile, being roughly uniform between the sub-cloud layer
 341 and about 263K and then decreasing at colder temperatures. The density increases more
 342 slowly as the SST is increased than in the K03 simulations (triangles in Figure 6a), but
 343 the changes in the PDFs are similar (Figure 4b), with the slope decreasing and the cut-
 off values increasing.



334 **Figure 6.** a) Average cloud density (q_c) as a function of SST for the small domain simulations
 335 with the single-moment scheme and the K03 parameter settings (black circles), the simulations
 336 with the NA5 parameter settings (black triangles) and the simulations with the M05 scheme (red
 337 diamonds). b) Same for the small domain K03 simulations with horizontal grid spacing of 0.5km
 338 (squares), 1km (circles) and 2km (triangles).

345 In the M05 simulations there is more liquid cloud water than cloud ice because the
 346 microphysics maintains more supercooled water (not shown), but the ratio of these stays
 347 constant across the simulations (Figure 2c). The mass of graupel increases slightly as
 348 the SST is increased, and the mass of rain again increases rapidly, going from roughly
 349 8 gm^{-2} to 40 gm^{-2} , but the mass of snow decreases substantially, going from about 40
 350 gm^{-2} at 290K to 15 gm^{-2} at 310K (Figure 2f). This decrease in the mass of snow is re-
 351 sponsible for the non-monotonicity in α , as the mass of cloud ice stays fixed.

352 The profiles of q_c and of the precipitation source are similar to those in the NA5
 353 simulations (Figure 6g and h), and the increase in liquid precipitation is again due to
 354 an increase in the range of altitudes with thick liquid clouds. However, in the M05 sim-
 355 ulations the peak in the precipitation source is higher in the atmosphere than in the NA5
 356 simulations, and in the coldest simulations it is above the freezing line. So the amount
 357 of snow decreases as the SST increases because the peak moves to warmer temperatures.
 358 That the peak is at colder temperatures in the M05 simulations despite the similar q_c

359 profiles implies that precipitation tends to form at colder temperatures in the Morrison
 360 scheme than in the single-moment scheme. The mass of cloud ice is roughly constant,
 361 as a decrease in the coverage of anvil clouds with surface warming is offset by an increase
 362 in their density (Figure 3i), but these clouds form little snow because their densities are
 363 still low.

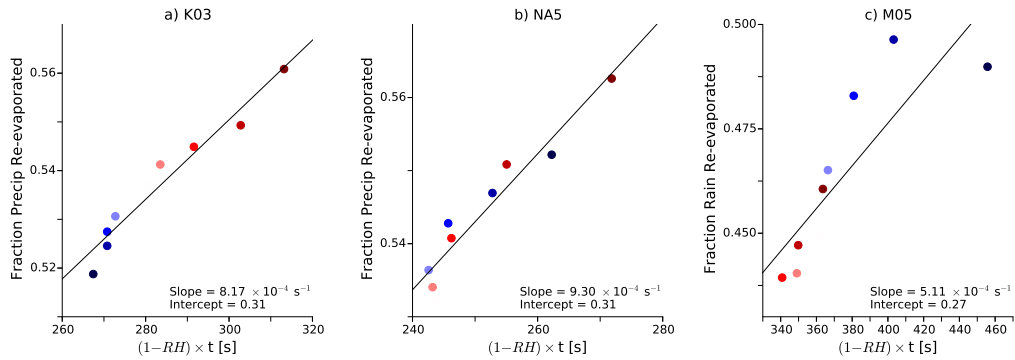
364 **3.3 Changes in precipitation evaporation**

365 A number of factors influence the re-evaporation of falling precipitation, and the
 366 roles these factors play are often not straightforward. For example, when hydrometeors
 367 fall faster there is less time for them to be re-evaporated, but this also increases the “ven-
 368 tilation factor” [Lin *et al.*, 1983], which promotes their evaporation. So faster fall speeds
 369 act to both reduce and enhance re-evaporation.

370 Nevertheless, as a first approximation we suggest that the fraction of falling pre-
 371 cipitation that is re-evaporated (β) scales as the saturation deficit times the average fall
 372 time:

$$\beta \sim (1 - RH) \times t = (1 - RH) \times h/w, \quad (6)$$

373 where RH is the relative humidity and t is the average fall time, equal to the average
 374 height at which precipitation forms (h) divided by the average fall speed (w).



375 **Figure 7.** a) $(1 - RH) \times t$ versus β for the small domain simulations with the single-moment
 376 scheme and the K03 parameter settings. The markers are colored by the underlying SST, with
 377 colder simulations blue and warmer simulations red. The line shows a linear least-squares fit. b)
 378 $(1 - RH) \times t$ versus β for the simulations with the NA5 parameter settings. c) $(1 - RH) \times t$ versus
 379 β for the M05 simulations.

380 This scaling is tested in Figure 7. RH is calculated as the mean relative humid-
 381 ity weighted by the mass of falling precipitation at each level:

$$RH = \frac{\overline{RHq_p}}{\overline{q_p}}, \quad (7)$$

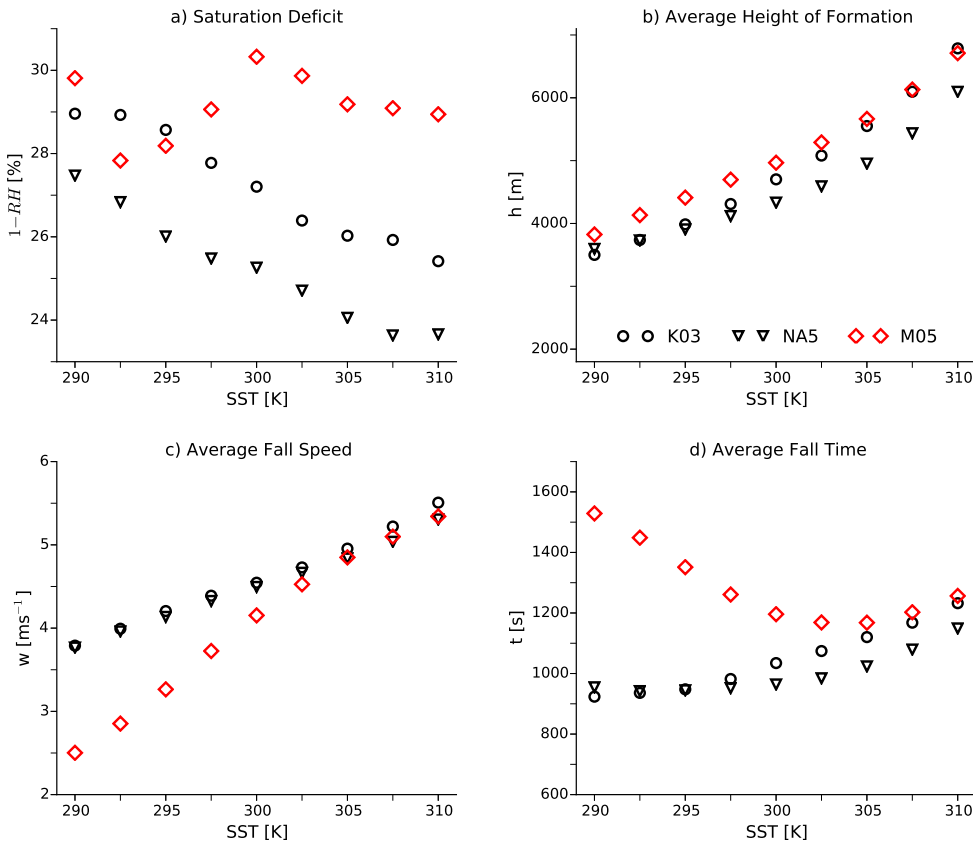
382 where the overlines denote domain averages and q_p now denotes the sum of the mixing
 383 ratios of all precipitating species. The average height at which precipitation forms is cal-
 384 culated from the source term in the precipitation equation, and the average fall speed
 385 of the precipitation is calculated as the mean fall speed weighted by the precipitation
 386 at each level, similar to the relative humidity

$$w = \frac{\overline{wq_p}}{\overline{q_p}}. \quad (8)$$

392 The scaling works well for the three sets of simulations, though the slopes differ (Fig-
 393 ure 7). The spread around the scaling is largest for the M05 simulations, which likely
 394 reflects differences in the microphysics controlling how rain and snow are evaporated in
 395 the double-moment scheme that are not accounted for in our scaling. The slope for these
 396 simulations is also smaller, indicating that precipitation is evaporated less efficiently in
 397 this scheme for the same fall time and saturation deficit, which partly explains why the
 398 sedimentation efficiencies are greater in this scheme (Figure 1c).

399 Figure 8 shows how the terms that go into equation (6) vary with SST. The two
 400 sets of single-moment simulations are very similar: the saturation deficit decreases as the
 401 SST increases (Figure 8a), while the heights and the fall speeds increase as the SST in-
 402 creases (Figures 8b and 8c, respectively), but the heights increase faster than the speeds,
 403 so the total fall time increases with warming in both sets of simulations (Figure 8d). The
 404 anti-correlation between the saturation deficit and the precipitation efficiency is notable,
 405 given the lower bound on ϵ in equation 2.

406 In the M05 simulations the saturation deficit changes non-monotonically, decreas-
 407 ing from 290K to 292.5K, then increasing up to 300K before decreasing again. The for-
 408 mation heights are similar to the single-moment simulations, while the fall speeds are
 409 much slower in the colder simulations (2.5ms^{-1} versus 3.75ms^{-1} at 290K), because the
 410 M05 simulations have more snow (which falls more slowly than rain). But the fall speeds
 411 increase rapidly as the amount of snow decreases, and from 302.5K on the fall speeds
 412 are almost the same in the three sets of simulations. The result is that the fall times in

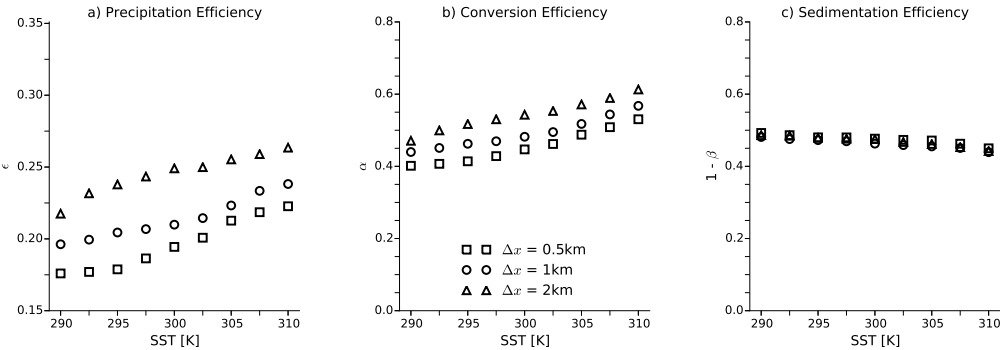


387 **Figure 8.** a) $(1 - RH)$ for the small domain simulations with the single-moment scheme and
 388 the K03 parameter settings (black circles), for the NA5 simulations (black triangles) and for the
 389 M05 simulations (red diamonds). b) Average height at which precipitation forms (h) for the same
 390 simulations. c) Average precipitation fall speeds (w) for the same simulations. d) Average fall
 391 time (t) for the same simulations.

413 the M05 simulations decrease from 290K to 302.5K, before increasing again in the warmest
 414 simulations.

415 Returning to Figure 1c, the sedimentation efficiency decreases in the K03 simula-
 416 tions as the SST increases because the fall time increases faster than the saturation deficit
 417 decreases, so more precipitation is re-evaporated. In the NA5 simulations the saturation
 418 deficit decreases faster than the fall time for the colder simulations, so $1 - \beta$ increases
 419 at first, and then the fall time increases faster for the warmer simulations and $1 - \beta$ de-
 420 creases. In the M05 simulations the large decreases in the fall speed in the colder sim-

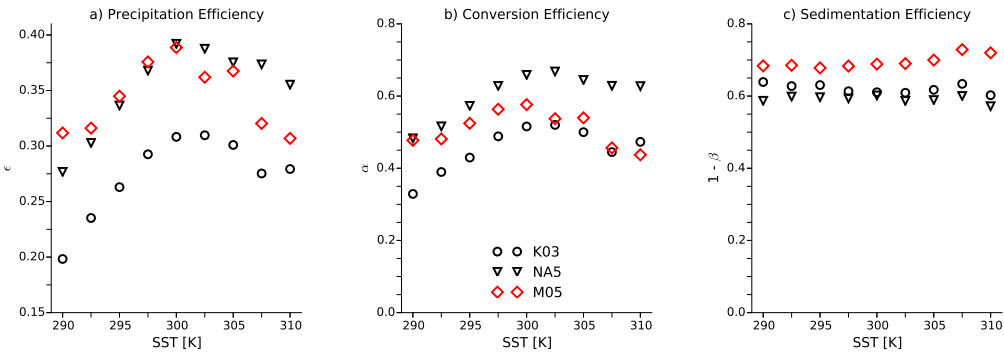
421 ulations causes $1 - \beta$ to increase for SSTs up to 302.5K, and then it decreases in the warmest
 422 simulations when the precipitation is dominated by rain.



423 **Figure 9.** a) The precipitation efficiency ϵ as a function of SST for the three sets of small do-
 424 main simulations with the K03 scheme in which the grid size is varied. Triangles show the results
 425 with a grid spacing of 0.5km, circles show results with a grid spacing of 1km and squares show
 426 results with a grid spacing of 2km. b) The conversion efficiency α as a function of SST for the
 427 same simulations. c) The sedimentation efficiency $1 - \beta$ as a function of SST.

428 3.4 Sensitivity to Resolution

429 The left panel of Figure 9 compares the precipitation efficiencies in simulations with
 430 the K03 microphysics and grid sizes of 0.5km, 1km and 2km. The efficiencies are sim-
 431 ilar, but decrease as the grid-size decreases. Comparing the center and right panels of
 432 the figure, this is mostly because the conversion efficiency decreases as the grid-size de-
 433 creases, with the re-evaporation decreasing slightly for finer grid sizes. Figure 6b shows
 434 that the average cloud density decreases as the grid-size decreases, which we believe is
 435 the main cause of the reduced conversion efficiency. We have not explored the reasons
 436 for the reduced cloud density when using finer grids, but hypothesize that the rate of en-
 437 trainment of environmental air into convecting plumes increases as the grid-size decreases,
 438 reducing the cloud condensate mixing ratios. Using Equation 6 shows that the primary
 439 cause of the reduced re-evaporation at finer grid-sizes is reductions in the saturation deficit
 440 for a given SST (not shown).



441 **Figure 10.** a) The precipitation efficiency ϵ as a function of SST for the three sets of 2D
 442 Walker simulations. Black circles show the K03 simulations, black triangles show the NA5 sim-
 443 ulations and red diamonds show the simulations with the M05 scheme. b) The conversion effi-
 444 ciency α as a function of SST for the same simulations. c) The sedimentation efficiency $1 - \beta$ as a
 445 function of SST.

446 4 2D Mock-Walker Simulations

447 The precipitation efficiencies for the 2D mock-Walker simulations are shown in the
 448 left panel of Figure 10. These have a similar range of values to the small domain sim-
 449 ulations, varying between 0.2 and 0.4, but do not increase monotonically with SST. In-
 450 stead the precipitation efficiencies increase with warming up to 300K and then decrease.

451 This progression is mostly due to the conversion efficiency (middle panel of Fig-
 452 ure 10), which follows the same pattern as ϵ , increasing in the K03 simulations from 0.32
 453 at 290K to 0.51, in the NA5 simulations from 0.51 to 0.68 and in the double-moment sim-
 454 ulations from 0.47 to 0.6; before decreasing again. The changes in $1 - \beta$ are small com-
 455 pared to these large changes. Both α and β are smaller than in the corresponding small-
 456 domain simulations, which is why the values of ϵ are comparable to those in the small-
 457 domain simulations, and ϵ is again smallest in the K03 simulations, though it is now com-
 458 parable in the NA5 and M05 simulations. Using Equation 6 shows that the sedimen-
 459 tation efficiency is larger in these simulations than in the small domain simulations because
 460 the relative humidity in the precipitating regions is higher and hence the saturation deficit
 461 is lower.

462 The changes in the conversion efficiency α reflect substantial changes in the organ-
 463 izations of the convection. For instance, the subsidence fraction decreases by $\sim 15\%$ when

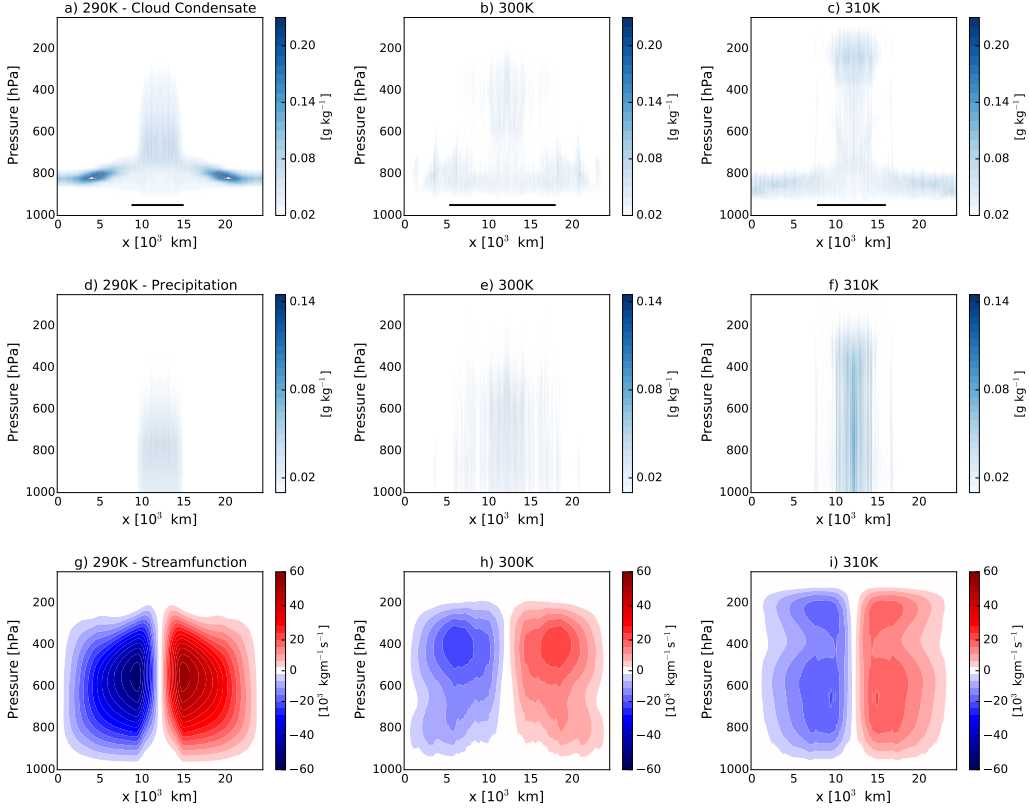
464 going from 290K to 297.5K with all three schemes, and increases at warmer SSTs (right
 465 panel of Figure 5)². The top panels of Figure 11 show how the cloud distributions in the
 466 K03 simulations are affected by these changes. In the coldest and warmest simulations,
 467 the clouds have a bimodal distribution, with narrow regions of deep convection over the
 468 warmest SSTs and low clouds decks outside these regions (Figures 11a and c). In the 300K
 469 case the strongest convection is still over the warmer SSTs, but it is less intense than in
 470 the other simulations and the low cloud decks are less well defined, with evidence of con-
 471 vective activity even over the colder SSTs. [The corresponding NA5 and M05 simula-
 472 tions are very similar.]

473 Although the low clouds have large cloud condensate mixing ratios, especially in
 474 the 290K case, they have small precipitation efficiencies. The reason for this can be seen
 475 from Figure 12, which shows profiles of the “regional” precipitation efficiency (top panel),
 476 conversion efficiency (middle panel) and sedimentation efficiency (bottom panel) for the
 477 290K, the 300K and the 310K mock-Walker simulations with the K03 simulations. These
 478 profiles were calculated by averaging the efficiencies over 192km blocks ³. In the 290K
 479 case, the precipitation efficiency is large (>0.4) in the convecting region and small ($<$
 480 0.1) in the subsidence region, reflecting differences in the conversion efficiency, though
 481 the sedimentation efficiency is also small over the coldest SSTs. The small conversion
 482 efficiency of the low clouds can also be seen by comparing Figure 11a and d, as the low
 483 clouds have large cloud condensate mixing ratios, but little precipitation.

484 In the 300K case the efficiencies are fairly uniform across the domain, while in the
 485 310K case the precipitation efficiency is large in the region of ascent and small in the re-
 486 gion of subsidence. In this case the small precipitation efficiency of the low clouds is en-
 487 tirely due to their conversion efficiency, as the sedimentation efficiency is large everywhere.
 488 Interestingly, the precipitation efficiency of the deep convection is relatively constant across
 489 the simulations, though it is slightly smaller in the 310K case than in the other two cases,
 490 and in the 290K case there is a peak in the center of the domain (though we note that
 491 the values are sensitive to the averaging period).

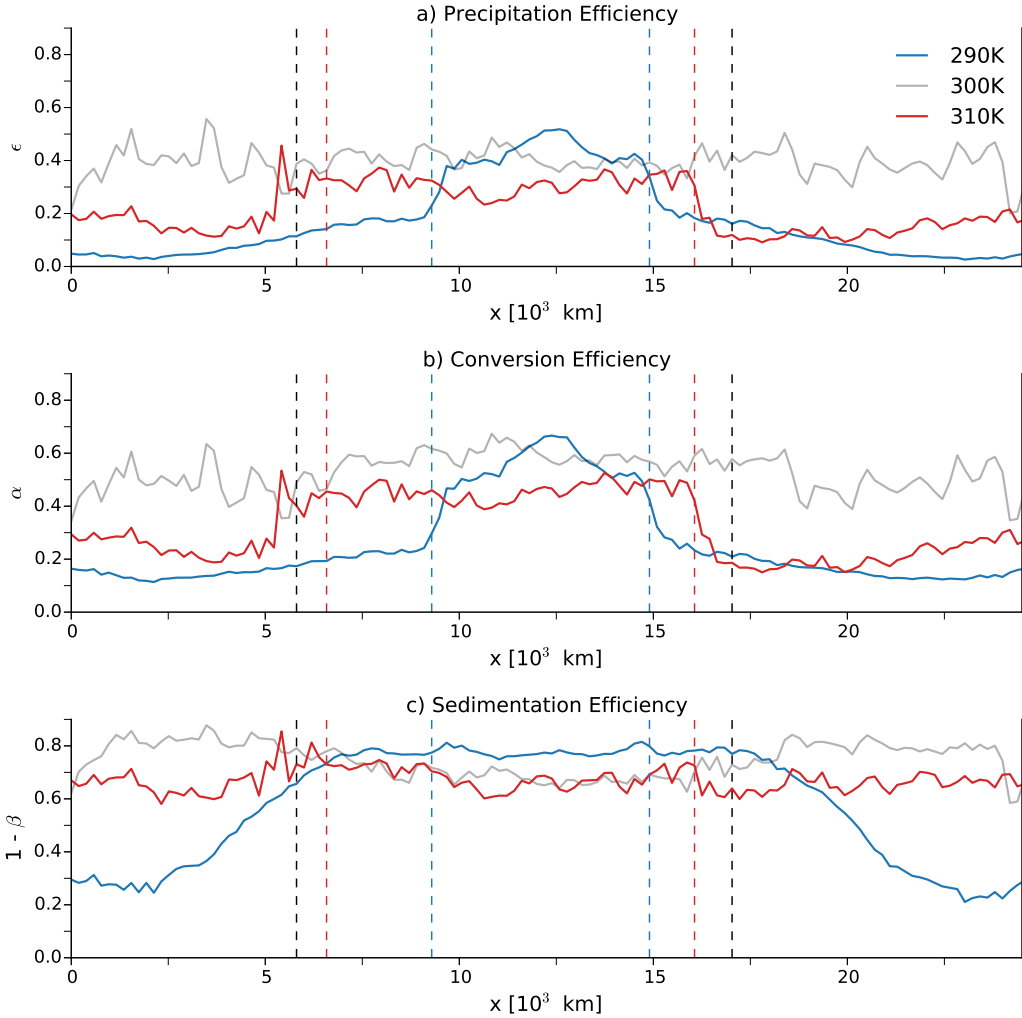
² As in *Cronin and Wing [2017]*, the subsidence fraction is calculated in the 2D Walker simulations by coarse-graining the data into 96km blocks.

³ Note that the domain-average efficiencies are not equal to the average of the regional efficiencies, as these must first be weighted by the local condensation and precipitation.



473 **Figure 11.** Top row: the time-mean cloud condensate mixing ratios (q_n) in the 290K sim-
 474 ulation (a), the 300K simulation (b) and the 310K simulation (c). Middle row: same for the
 475 time-mean precipitation mixing ratios (q_p). Bottom row: same for the time-mean overturning
 476 streamfunction, which is calculated as $s(p, x) = \frac{1}{g} \int_{p_s}^p u(p', x) dp$, where u is the horizontal veloc-
 477 ity.

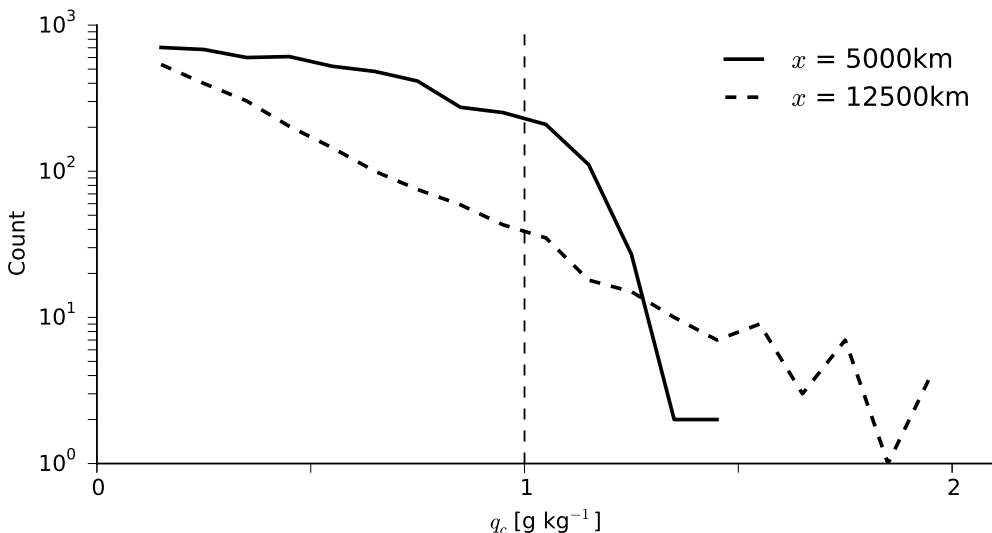
506 To understand the differences in conversion efficiency between the low and high clouds,
 507 Figure 13 shows PDFs of q_c for the 290K simulation with the K03 scheme for a region
 508 of low cloud cover (solid line) and for the center of the domain (dashed line). The PDFs
 509 are estimated for the altitudes of maximum time-mean q_c at each location. In the low
 510 cloud region there is a very sharp cut-off near $q_{c,0}$, and there are no extreme events dur-
 511 ing which substantial amounts of precipitation are formed. This may be related to the
 512 presence of very dry air just above the low clouds, as mixing with the dry air could in-
 513 hibit the low clouds from becoming overly dense. Conversely, in the region of deep con-
 514 vection the average cloud density is lower, but the distribution is broader and there are



489 **Figure 12.** a) Profiles of the precipitation efficiency ϵ in the 290K, 300K and 310K mock-
 490 Walker simulations with the K03 scheme. The values of ϵ are averaged over 192km blocks and
 491 the dashed lines separate regions of subsidence from regions of ascent. b) Profiles of the conver-
 492 sion efficiency α from the same simulations. c) Profiles of the sedimentation efficiency $1 - \beta$ from
 493 the same simulations.

515 periods during which the clouds become very dense and large amounts of precipitation
 516 are formed.

517 So α increases when going from 290K to 300K because of the erosion of the low cloud
 518 decks, and then decreases as the low clouds reform with surface warming from 300K to
 519 310K. This progression is associated with changes in the large-scale circulation, which
 520 goes from a single, large overturning cell in the coldest simulations to a double-cell struc-



502 **Figure 13.** Probability density functions of q_c in the 290K 2D Walker simulations with the
 503 K03 scheme. The solid curve shows the values at the altitude of maximum time-mean q_c at x
 504 = 5000km and the dashed curve shows values at the altitude of maximum time-mean q_c at $x =$
 505 12500km.

521 ture in the warmest cases (bottom panels of Figure 11). We are actively investigating
 522 the reasons for these changes in the circulation, but for now we note that there are large
 523 changes in the strength of the subsidence as part of this transition. In the 290K case the
 524 strong subsidence creates a stronger inversion and hence more low cloud cover over the
 525 colder SSTs. In the intermediate cases the subsidence is weaker, leading to a weaker in-
 526 version over the cold part of the domain and more convection. There is strong subsidence
 527 over the coldest SSTs in the warmest cases, and the low cloud decks return.

528 5 Summary and Conclusion

529 We have investigated how the precipitation efficiency, ϵ , varies in CRM simulations
 530 of RCE as the mean underlying SST is varied from 290K to 310K. We have considered
 531 three different microphysics schemes and two set-ups: a small, doubly-periodic domain
 532 and a wide 2D domain with a sinusoidal SST profile, whose gradient approximately matches
 533 the zonal SST gradient in the equatorial Pacific. In the small domain simulations the
 534 precipitation efficiency generally increases with warming because clouds become denser
 535 in warmer climates and so cloud condensate is converted more efficiently into precipi-
 536 tation. Changes in the re-evaporation of precipitation are small, though the sedimen-

tation efficiency does tend to increase in warmer climates. In the double-moment simulations there is an added complication because of large reductions in the amount of snow with warming for SSTs lower than 300K. In this scheme snow re-evaporates much more readily than rain because of its slower fall speeds, and so the reduction in snow tends to cause the precipitation efficiency to increase, except for when going from 290K to 292.5K. We have found that these results are not qualitatively sensitive to the grid size of the simulations, though the precipitation efficiency decreases at finer resolutions because the cloud density decreases.

The precipitation efficiency is not monotonic in the 2D Walker simulations, as it increases up to about 300K and then decreases with further warming. This reflects a local minimum in the strength of the large-scale circulation, and consequently in the organization of convection as well, around 300 K. Low cloud fraction in subsidence regions tends to correlate with the strength of the overturning circulation, and thus is minimized for surface temperatures near 300K. Since low clouds have small precipitation efficiencies (≤ 0.1), the global precipitation efficiency is largest when the surface temperature is 300K, and smaller for both warmer and colder surfaces.

These results can be summarized as saying that, all else equal, the precipitation efficiency increases with surface warming, but may decrease due to changes in the abundances of the different precipitating phases or in the degree of convective organization. With regards to the latter, we have actually found the opposite effect of convective aggregation on precipitation efficiency than what has previously been proposed: instead of an increase in precipitation efficiency with convective aggregation, increased clustering of convection is associated with an expansion of low cloud decks, which have very small precipitation efficiencies and so the domain-mean precipitation efficiency decreases. We have found no evidence that the precipitation efficiency in the region of strong convection increases with increased clustering.

Our results are a first step towards understanding the sensitivity of the bulk precipitation efficiency of convection to the underlying surface temperature, and should be supplemented by future work involving high-resolution process modeling and observational analysis to further constrain how precipitation efficiency is best parameterized in GCMs. Our results also point to the importance of accurately modelling the vertical distributions of the different water phases, especially capturing the temperatures at which

569 precipitation forms. *Jiang et al.* [2012] have shown that climate models tend to overestimate
 570 the amount of liquid water relative to frozen water in the tropical atmosphere,
 571 which could be an important source of error in the representation of the precipitation
 572 efficiency of tropical clouds.

573 Returning to the issue of clouds and climate sensitivity, the mock-Walker simulations
 574 suggest caution in linking changes in precipitation efficiency and low cloud cover,
 575 as any microphysical effects can be overwhelmed by changes in the large-scale tropical
 576 circulation. Moreover, low clouds in GCMs may have unrealistically large precipitation
 577 efficiencies (e.g., GCMs are known to have a “drizzle” problem), and so the GCMs’ climates
 578 could be overly sensitive to changes in these precipitation efficiencies. On the other
 579 hand, the large circulation changes in our mock-Walker simulations may be masking subtle
 580 effects related to changes in precipitation efficiency, which would show up in more realistic
 581 models whose tropical circulation is not so sensitive. Continuing to untangle the
 582 relationship between cloud microphysics and the tropical circulation is a major task for
 583 tropical dynamics.

584 A: Scaling of Sensitivity of Cloud Liquid Water Content To Temperature

586 *Betts and Harshvardhan* [1987] showed that for liquid water clouds formed by undilute
 587 ascent along a saturated moist adiabat, the fractional change in the cloud liquid water
 588 content between two fixed heights z_1 and z_2 per degree temperature change is:

$$f_u = \frac{1}{l} \left(\frac{\partial l}{\partial T} \right)_{z_1, z_2} = \frac{1}{\Gamma_{\theta, m}} \frac{\partial \Gamma_{\theta, m}}{\partial T}, \quad (\text{A.1})$$

589 where $\Gamma_{\theta, m}$ is the gradient of potential temperature θ along the moist adiabat and l is
 590 the liquid water content of a cloud between z_1 and z_2

$$l \approx \left\langle \left(\frac{\partial q_v^*}{\partial z} \right)_{\theta_{e,s}} \right\rangle \Delta z, \quad (\text{A.2})$$

591 with q_v^* the saturation mixing ratio along the moist adiabat (i.e., along constant $\theta_{e,s}$),
 592 $\Delta z = z_2 - z_1$ and the angle brackets denoting an average over Δz . This relationship
 593 is approximate because it represents a linearization. f_u is always less than or equal to
 594 the Clausius-Clapeyron scaling $\frac{1}{q_v^*} \frac{\partial q_v^*}{\partial T}$ and the difference between this scaling and the CC
 595 scaling increases as the temperature increases, with a more complex dependence on pressure.
 596 For a cloud base at 800hPa and a temperature of 278.15K f is $4.1\%K^{-1}$ [*Betts and*
597 Harshvardhan, 1987].

To examine how equation A.1 is affected by entrainment we consider the plume equation for an entraining plume under the zero buoyancy approximation [Singh and O'Gorman, 2013]

$$\frac{dh_e^*}{dz} = -\varepsilon L_v (q_{v,e}^* - q_{v,e}), \quad (\text{A.3})$$

where h_e^* is the saturated moist static energy of the plume, ε is the entrainment rate, L_v is the latent heat of vaporization, $q_{v,e}^*$ is the saturated specific humidity of the plume and $q_{v,e}$ is the mixing ratio of the environment. Subscript e denotes the environment and moist static energy $h = c_p T + gz + L_v q_v$, with c_p the specific heat capacity of air and g the gravitational constant. The zero-buoyancy assumption sets the temperature of the plume equal to the environmental temperature $T^* = T_e$ and so $q_v^* = q_{v,e}^*$.

This expression can be re-arranged to give an expression for the water vapor lapse-rate γ^* in the plume:

$$\gamma^* = -\frac{c_p}{L_v} \Gamma_e - \frac{g}{L_v} - \varepsilon L_v (1 - RH) q_{v,e}^*, \quad (\text{A.4})$$

where RH is the relative humidity and Γ_e is the environmental temperature lapse-rate.

The budget for the total water in the plume is

$$\frac{dq_t}{dz} = \frac{d(q_{v,e}^* + q_c)}{dz} = -\varepsilon (q_c + (1 - RH) q_{v,e}^*), \quad (\text{A.5})$$

where q_c is the condensed water in the plume and we assume there is no fallout of hydrometeors. Substituting for $\frac{dq_{v,e}^*}{dz}$ from equation A.4 and re-arranging then gives

$$\frac{dq_c}{dz} = \frac{c_p}{L_v} \Gamma_e + \frac{g}{L_v} - \varepsilon q_c. \quad (\text{A.6})$$

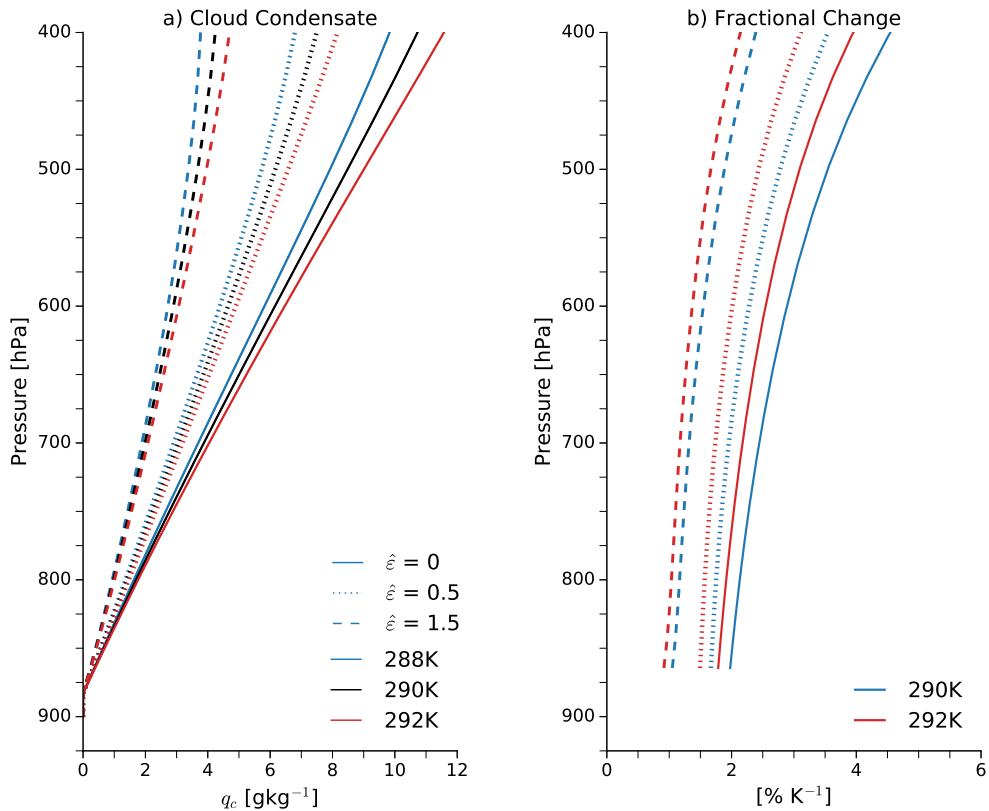
This equation can be solved by multiplying across by $e^{\int \varepsilon dz}$ and integrating to give

$$q_c(z') = \frac{1}{e^{\int_{zcb}^{z'} \varepsilon dz}} \left[\int_{zcb}^{z'} \left(\frac{c_p}{L_v} \Gamma_e + \frac{g}{L_v} \right) e^{\int_{zcb}^{z'} \varepsilon dz} dz \right], \quad (\text{A.7})$$

where zcb is the height of the cloud base. Note that in addition to appearing explicitly in this equation, ε also appears implicitly through its influence on the environmental lapse-rate Γ_e [Singh and O'Gorman, 2013].

To illustrate the effects of entrainment on the cloud condensate mixing ratio, Figure A.1 plots profiles of q_c calculated using equation A.7, for plumes originating at 900hPa with three different temperatures and an environmental $RH = 80\%$. We also follow Singh and O'Gorman in setting $\varepsilon = \hat{\varepsilon}/z$ and perform the calculations using $\hat{\varepsilon} = 0$ (i.e., undilute ascent), 0.5 and 1.5. Panel a) of the Figure shows that the cloud condensate mixing ratio increases with the cloud-base temperature and decreases significantly with $\hat{\varepsilon}$.

623 Panel b) shows the fractional change in the mixing ratio as the cloud-base temperature
 624 is increased. As in Betts and Harshvardhan, the fractional change decreases as the cloud-
 625 base temperature increases, and again the entrainment has a strong effect, substantially
 626 reducing the fractional change. From this we infer that, assuming entrainment rates are
 627 not affected by temperature, the fractional change in q_c for a dilute plume will be greater
 628 than zero, but less than the fractional increase of an undilute plume.



629 **Figure A.1.** a) Cloud condensate mixing ratios for plumes starting at 900hPa with an en-
 630 vironmental relative humidity of 80% and cloud-base temperature of 288K (blue), 290K (black)
 631 and 292K (red), calculated using equation A.7. The solid lines assume no entrainment, the dot-
 632 ted lines include entrainment with $\hat{\varepsilon}$ of 0.5 and the dashed lines include entrainment with $\hat{\varepsilon}$ of
 633 1.5. b) Fractional change in cloud condensate mixing ratio when increasing the cloud-base tem-
 634 perature from 288 to 290K (blue lines) and from 290K to 292K (red lines). The solid, dotted and
 635 dashed lines have the same meaning as in panel a).

636 **Acknowledgments**

637 We thank Tom Beucler and Kerry Emanuel for helpful comments on earlier drafts of the
 638 manuscript and the NSF for support through grant AGS-1623218, “Collaborative Re-
 639 search: Using a Hierarchy of Models to Constrain the Temperature Dependence of Cli-
 640 mate Sensitivity”.

641 **References**

- 642 Bailey, A., J. Nusbaumer, and D. Noone (2015), Precipitation efficiency derived
 643 from isotope ratios in water vapor distinguishes dynamical and microphysical in-
 644 uences on subtropical atmospheric constituents, *Journal of Geophysical Research: Atmo-*
 645 *spheres*, 120(23), 9119–9137.
- 646 Beheng, K. D. (1994), A parameterization of warm cloud microphysical conversion
 647 processes., *Atmospheric Research*, 33(23), 193–206.
- 648 Betts, A. K., and Harshvardhan (1987), Thermodynamic constraint on the cloud
 649 liquid water feedback in climate models, *Journal of Geophysical Research: Atmo-*
 650 *spheres*, 92(D7), 8483–8485.
- 651 Coppin, D., and S. Bony (2015), Physical mechanisms controlling the initiation of
 652 convective self-aggregation in a general circulation model., *Journal of Advances in*
 653 *Modeling Earth Systems*, 7(23), 2060–2078.
- 654 Cronin, T. W., and A. A. Wing (2017), Clouds, circulation, and climate sensitiv-
 655 ity in a radiative-convective equilibrium channel model., *Journal of Advances in*
 656 *Modeling Earth Systems*, 9(5), 2883–2905.
- 657 Emanuel, K., A. A. Wing, and E. M. Vincent (2014), Radiative-convective in-
 658 stability, *Journal of Advances in Modeling Earth Systems*, 6(1), 75–90, doi:
 659 10.1002/2013MS000270.
- 660 Emanuel, K. A. (1987), An air-sea interaction model of intraseasonal oscillations in
 661 the tropics., *Journal of the Atmospheric Sciences*, 44(23), 2324–2340.
- 662 Emanuel, K. A., and M. Bister (1996), Moist convective velocity and buoyancy
 663 scales., *Journal of the Atmospheric Sciences*, 53(23), 3276–3285.
- 664 Harrop, B. E., and D. L. Hartmann (2016), The role of cloud radiative heating
 665 within the atmosphere on the high cloud amount and topofatmosphere cloud ra-
 666 diative effect, *Journal of Advances in Modeling Earth Systems*, 8(23), 1391–1410.

- 667 Jiang, J. H., S. Hui, Z. Chengxing, P. V. S., D. G. Anthony, N. L. S., D. L. J.,
668 H. Larry, S. Charles, C. Jason, G. Andrew, R. M. A., R. Leon, J. Stephen,
669 W. Tongwen, B. Florent, D. JeanLouis, K. Hideaki, K. Tsuyoshi, W. Masahiro,
670 L. T. S., V. E. M., I. Trond, D. Helge, M. M. D. S., R. W. G., W. J. W., T. Bai-
671 jun, T. Joao, and S. G. L. (2012), Evaluation of cloud and water vapor simula-
672 tions in cmip5 climate models using nasa atrain satellite observations, *Journal of*
673 *Geophysical Research: Atmospheres*, 117(D14).
- 674 Khairoutdinov, M. F., and D. A. Randall (2003), Cloud resolving modeling of the
675 arm summer 1997 iop: Model formulation, results, uncertainties, and sensitivities,
676 *Journal of the Atmospheric Sciences*, 60(23), 607–625.
- 677 Langhans, W., K. Yeo, and D. M. Romps (2015), Lagrangian investigation of the
678 precipitation efficiency of convective clouds, *Journal of the Atmospheric Sciences*,
679 72(3), 1045–1062.
- 680 Lau, K. M., and H. T. Wu (2003), Warm rain processes over tropical oceans and
681 climate implications., *Geophysical Research Letters*, 30(3), 2290.
- 682 Lin, Y. L., R. D. Farley, and H. D. Orville (1983), Bulk parameterization of the
683 snow field in a cloud model., *Journal of Applied Meteorology and Climatology*,
684 22(23), 1065–1092.
- 685 Lopez, M. A., D. L. Hartmann, P. N. Blossey, R. Wood, C. S. Bretherton, and T. L.
686 Kubar (2009), A test of the simulation of tropical convective cloudiness by a cloud
687 resolving model, *Journal of Climate*, 22(11), 2834–2849.
- 688 Marshall, J. S., and W. K. Palmer (1948), The distribution of raindrops with size.,
689 *Journal of Meteorology*, 5(23), 165–166.
- 690 Mauritsen, T., and B. Stevens (2015), Missing iris effect as a possible cause of muted
691 hydrological change and high climate sensitivity in models, *Nature Geoscience*,
692 8(346), 346–351.
- 693 Mauritsen, T., B. Stevens, E. Roeckner, T. Crueger, M. Esch, M. Giorgetta,
694 H. Haak, J. Jungclaus, D. Klocke, D. Matei, U. Mikolajewicz, D. Notz, R. Pin-
695 cius, H. Schmidt, and L. Tomassini (2012), Tuning the climate of a global model,
696 *Journal of Advances in Modeling Earth Systems*, 4(3), 1–18.
- 697 Morrison, H., J. A. Curry, and V. I. Khvorostyanov (2005), A new double-moment
698 microphysics parameterization for application in cloud and climate models. part i:
699 Description, *Journal of the Atmospheric Sciences*, 62(23), 1665–1677.

- 700 Pauluis, O., and I. M. Held (2002a), Entropy budget of an atmosphere in radiative-
701 convective equilibrium. part ii: Latent heat transport and moist processes, *Journal*
702 *of the Atmospheric Sciences*, 59(59), 140–149.
- 703 Pauluis, O., and I. M. Held (2002b), Entropy budget of an atmosphere in radiative-
704 convective equilibrium. part i: Maximum work and frictional dissipation, *Journal*
705 *of the Atmospheric Sciences*, 59(59), 125–139.
- 706 Raymond, D. J., S. L. Sessions, A. H. Sobel, and Z. Fuchs (2009), The mechanics
707 of gross moist stability, *Journal of Advances in Modeling Earth Systems*, 1(3),
708 doi:10.3894/JAMES.2009.1.9.
- 709 Rennó, N. O., and A. P. Ingersoll (1996), Natural convection as a heat engine: A
710 theory for cape., *Journal of the Atmospheric Sciences*, 53(23), 572–585.
- 711 Romps, D. M. (2011), Response of tropical precipitation to global warming., *Journal*
712 *of the Atmospheric Sciences*, 68(23), 123–138.
- 713 Romps, D. M. (2014), An analytical model for tropical relative humidity., *Journal of*
714 *Climate*, 27(23), 7432–7449.
- 715 Sherwood, S. C., S. Bony, and J.-L. Dufresne (2014), Spread in model climate sensi-
716 tivity traced to atmospheric convective mixing, *Nature*, 505, 37–42.
- 717 Singh, M. S., and P. A. O’Gorman (2013), Influence of entrainment on the ther-
718 mal stratification in simulations of radiative-convective equilibrium, *Geophysical*
719 *Research Letters*, 40(3), 4398–4403.
- 720 Sui, C. H., X. Li, M. J. Yang, and H. L. Huang (2007), On the definition of precipi-
721 tation efficiency., *Journal of the Atmospheric Sciences*, 64(23), 4506–4513.
- 722 Tao, W. K., D. Johnson, C. L. Shie, and J. Simpson (2004), The atmospheric energy
723 budget and large-scale precipitation efficiency of convective systems during toga
724 coare, gate, scsmex, and arm: Cloud-resolving model simulations., *Journal of the*
725 *Atmospheric Sciences*, 61(23), 2405–2423.
- 726 Tomassini, L., A. Voigt, and B. Stevens (2015), On the connection between tropical
727 circulation, convective mixing, and climate sensitivity, *Quarterly Journal of the*
728 *Royal Meteorological Society*, 9(141), 1404–1416.
- 729 Tompkins, A. M., and A. G. Semie (2017), Organization of tropical convection in
730 low vertical wind shears: Role of updraft entrainment., *Journal of Advances in*
731 *Modeling Earth Systems*, 9(23), 1046–1068.

- 732 Wing, A. A., and K. A. Emanuel (2014), Physical mechanisms controlling self-
733 aggregation of convection in idealized numerical modeling simulations, *Journal of*
734 *Advances in Modeling Earth Systems*, 6(1), 59–74.
- 735 Yano, J. I., and K. A. Emanuel (1991), An improved model of the equatorial tro-
736 posphere and its coupling with the stratosphere., *Journal of the Atmospheric*
737 *Sciences*, 48(23), 377–389.
- 738 Zhao, M. (2014), An investigation of the connections among convection, clouds,
739 and climate sensitivity in a global climate model., *Journal of Climate*, 68(27),
740 1845–1862.
- 741 Zhao, M., J.-C. Golaz, I. M. Held, S.-J. Lin, Y. Ming, P. Ginoux, B. Wyman, L. J.
742 Donner, D. Paynter, and H. Guo (2016), Uncertainty in model climate sensitiv-
743 ity traced to representations of cumulus precipitation microphysics, *Journal of*
744 *Climate*, 68(29), 543–560.